

Radio Science®

RESEARCH ARTICLE

10.1029/2025RS008350

Key Points:

- A MIMO antenna integrated with a frequency selective surface (FSS) is designed for 5G mm-Wave applications operating across an ultra-wide bandwidth of 22–46 GHz
- A key innovation lies in the integration of a FSS layer above the MIMO structure that significantly enhances the radiation characteristics
- The proposed FSS-based MIMO antenna offers a compact, high-efficiency, and wideband solution for next-generation 5G mm-Wave devices

Correspondence to:

M. Alibakhshikenari and N. A. Elmunim,
mohammad.alibakhshikenari@universityofgalway.ie;
naasmail@pnu.edu.sa

Citation:

Alibakhshikenari, M., Din, I. ud., Elmunim, N. A., Virdee, B. S., Kumar, S., Ullah, S., et al. (2025). High-performance multiport antenna with frequency selective surface for 5G Ka-band applications. *Radio Science*, 60, e2025RS008350. <https://doi.org/10.1029/2025RS008350>

Received 14 MAY 2025

Accepted 13 NOV 2025

Author Contributions:

Conceptualization:

Mohammad Alibakhshikenari, Nouf Abd Elmunim, Bal S. Virdee

Data curation:

Mohammad Alibakhshikenari, Iftikhar ud Din, Bal S. Virdee, Chan Hwang See

Formal analysis:

Mohammad Alibakhshikenari, Iftikhar ud Din, Ernesto Limiti, Takfarinas Saber

Funding acquisition:

Mohammad Alibakhshikenari, Nouf Abd Elmunim

Investigation:

Mohammad Alibakhshikenari, Nisar Ahmad Abbasi, Chan Hwang See


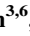


Methodology:

Mohammad Alibakhshikenari, Iftikhar ud Din, Sadiq Ullah, Muhammad Akmal Chaudhary

© 2025. The Author(s).

This is an open access article under the terms of the [Creative Commons Attribution License](#), which permits use, distribution and reproduction in any medium, provided the original work is properly cited.

High-Performance Multiport Antenna With Frequency Selective Surface for 5G Ka-Band Applications

Mohammad Alibakhshikenari^{1,2} , Iftikhar ud Din³, Nouf Abd Elmunim⁴, Bal S. Virdee⁵, Sunil Kumar⁵ , Sadiq Ullah^{3,6}, Muhammad Akmal Chaudhary⁷, Nisar Ahmad Abbasi⁸, Chan Hwang See⁹, Ernesto Limiti¹⁰ , and Takfarinas Saber¹ 

¹LERO, the Research Ireland Centre for Software, College of Science and Engineering, School of Computer Science, University of Galway, Galway, Ireland, ²Department of Electrical and Electronics Engineering, Dogus University, Istanbul, Türkiye, ³Telecommunication Engineering Department, University of Engineering and Technology, Mardan, Pakistan, ⁴Department of Electrical Engineering, College of Engineering, Princess Nourah bint Abdulrahman University, Riyadh, Saudi Arabia, ⁵Center for Communications Technology, London Metropolitan University, London, UK, ⁶Department of Electrical Engineering, Faculty of Engineering, University of Tabuk, Tabuk, Saudi Arabia, ⁷Department of Electrical and Computer Engineering, Ajman University, Ajman, United Arab Emirates, ⁸Department of Electrical Engineering, School of Systems Engineering, Bahrain Polytechnic, Isa Town, Bahrain, ⁹School of Computing, Engineering and the Built Environment, Edinburgh Napier University, Edinburgh, UK, ¹⁰Electronics Engineering Department, University of Rome “Tor Vergata”, Rome, Italy

Abstract This paper presents a novel multiport antenna tailored for 5G millimeter-wave (mm-Wave) applications. The proposed design features orthogonally arranged radiating elements to ensure compactness with an overall footprint of just $20 \times 26 \text{ mm}^2$. A key innovation is the integration of a frequency selective surface (FSS) layer placed above the antenna system to enhance gain and isolation without increasing complexity. This FSS enhances gain by 1.5 dB across the band, achieving a peak gain of 7.5 dBi at 41 GHz. The antenna operates across the entire Ka-band (22–46 GHz), delivering efficiency exceeding 80% and maintaining isolation above 20 dB. Key multiport antenna performance parameters including diversity gain ($DG = 10$) and envelope correlation coefficient ($ECC < 0.005$) align with performance benchmarks, and experimental measurements validate simulation results. The unique combination of orthogonal element placement and FSS enhancement positions this antenna as a robust solution for next-generation 5G applications.

1. Introduction

The fifth generation (5G) wireless communication standard has significantly enhanced network capacity by increasing data rates, supporting a higher number of simultaneous device connections, reducing latency, and improving energy efficiency while optimizing spectrum utilization (Hussain, et al., 2024; Iskandarani, 2024; Qasem, 2024). The 5 G spectrum is broadly categorized into two segments: sub-6 GHz and millimeter-wave (mm-Wave) frequencies (Rafique et al., 2022; Kiani et al., 2022; Luo et al., 2022).

Among these, mm-Wave frequencies, particularly in the Ka-band, are gaining significant attention due to their ability to support high-speed data transmission, high-resolution multimedia streaming, and large bandwidth availability (Dokmetas et al., 2024; Yusuf Onay & Dokmetas, 2025). These frequencies also enable the design of compact antenna arrays because of the shorter wavelengths involved. Additionally, mm-Wave systems offer advantages such as low interference, improved security, and cost-effective deployment (Desai et al., 2019; Hong, 2017).

To meet the ever-growing demand for data and connectivity, researchers are increasingly focused on mm-Wave multiport antenna systems. These systems can accommodate densely packed antenna arrays to boost throughput. However, a key challenge in compact multiport antenna design is managing the mutual coupling between closely spaced radiating elements, which can adversely affect gain and overall efficiency (Jilani & Alomainy, 2018; Shen et al., 2019). Solutions such as increasing inter-element spacing or incorporating isolation-enhancing structures like electromagnetic band gap (EBG) materials have been explored, although these often add complexity or require increased physical space (Madni et al., 2022).

Several advanced decoupling techniques have been proposed to tackle mutual coupling. For instance, meta-material absorbers and EBG structures have been employed to achieve isolation as high as 50 dB in 5.8 GHz

Project administration:

Mohammad Alibakhshikenari

Resources: Mohammad Alibakhshikenari, Iftikhar ud Din, Chan Hwang See

Software: Mohammad Alibakhshikenari, Iftikhar ud Din, Bal S. Virdee, Sunil Kumar

Supervision: Ernesto Limiti, Takfarinas Saber

Validation:

Mohammad Alibakhshikenari, Iftikhar ud Din, Nouf Abd Elmunim, Bal S. Virdee, Sunil Kumar, Sadiq Ullah, Muhammad Akmal Chaudhary, Nisar Ahmad Abbasi, Chan Hwang See, Ernesto Limiti, Takfarinas Saber

Visualization:

Mohammad Alibakhshikenari, Sadiq Ullah, Muhammad Akmal Chaudhary, Nisar Ahmad Abbasi

Writing – original draft:

Mohammad Alibakhshikenari, Iftikhar ud Din, Bal S. Virdee

Writing – review & editing:

Mohammad Alibakhshikenari, Iftikhar ud Din, Nouf Abd Elmunim, Bal S. Virdee, Sunil Kumar, Sadiq Ullah, Muhammad Akmal Chaudhary, Nisar Ahmad Abbasi, Chan Hwang See, Ernesto Limiti, Takfarinas Saber

WLAN systems (Pan et al., 2019; Sharma et al., 2023; Sokunbi & Attia, 2020). In one approach, three double F-shaped slots were etched into the ground plane of a patch array, enhancing isolation bandwidth by 48% and boosting isolation from 10 to 40 dB. Metallic vias and slot arrays with defected ground structures (DGS) have also proven effective in dielectric resonator Antennas (DRAs), achieving isolation improvements from 15.1 to 34.2 and 13.1 to 43 dB at 26 GHz (Pan et al., 2019; Sharma et al., 2023). Other designs utilize wheel-shaped absorbers or slot-coupled patches to reduce backward radiation and mutual coupling (Gao et al., 2020; Jang et al., 2019; Sokunbi et al., 2023; Zhang et al., 2019).

Metasurfaces and frequency selective surfaces (FSS) are emerging as powerful tools in multiport antenna design, offering compact and efficient ways to enhance gain, suppress surface waves, and improve radiation characteristics (Bao et al., 2022; Tian et al., 2021). For instance, dual-band metasurfaces have been shown to manipulate both reflected and transmitted wave phases, enhancing the end-fire gain of Vivaldi antennas by up to 73% at 28 GHz (Singh & Parihar, 2023). Antennas using metasurface loading have demonstrated gains up to 12 dB and improved phase uniformity, effectively compensating for atmospheric attenuation in mm-Wave systems (Munir et al., 2023; Sehrai et al., 2020; Tariq et al., 2021).

Notably, recent multiport antenna designs have also incorporated orthogonal orientation of elements, modified ground planes, and metasurface layers to achieve superior isolation (>20 dB), high efficiency (>80%), and broad bandwidth performance (Abbas et al., 2023). These designs reflect the ongoing trend of combining structural and electromagnetic optimization techniques to address mutual coupling and radiation efficiency challenges.

In this work, we propose a compact four-port microstrip antenna optimized for 5G mm-wave applications. The design follows a four-stage progression: starting from a single T-shaped patch, evolving to a U-shaped radiator with a modified ground, arranging orthogonal elements to suppress mutual coupling, and finally integrating a FSS superstrate at an optimized height to enhance gain and bandwidth. The resulting antenna operates effectively from 22 to 46 GHz, achieving isolation >20 dB, peak gain up to 7.5 dBi, and maximum total efficiency up to 93%.

Recent next-generation microstrip studies have improved gain/efficiency using metasurface (MS) superstrates and focusing MS layers, demonstrated dual-band mmWave multiport antenna at 28/38 GHz, and developed compact SIW-backed patches for FR2 front-ends. For example, MS-assisted microstrip designs deliver high-gain, dual-polarization, and broadband CP/LP operation in compact form factors (Sun et al., 2024). Dual-band printed/multiport antenna patches at 28/38 GHz enable practical arraying for 5 G/6G links, while SIW cavity-backed patches provide low-profile, high-Q radiators suited to integrated modules (Altakhaineh et al., 2023). Very recent work also combines MS structures with miniaturization to realize high-isolation multiport antenna and broadband, gain-enhanced patches (Hasan et al., 2024). Aligned with these directions, our prototype leverages FSS loading, wideband multiport antenna architecture, and efficiency optimization, contributing measured >80% efficiency across 22–46 GHz with 7.5 dBi peak gain, all supported by repeatability analysis and a fully characterized uncertainty budget.

The remainder of the paper is organized as follows. Section 2 presents the antenna design and its evolution. Section 3 describes the FSS structure and its integration with the antenna. Section 4 reports the simulated and measured results. Section 5 discusses the multiport antenna performance metrics. Section 6 provides a comparative analysis with recent literature, and Section 7 concludes the paper with final remarks.

2. Antenna Design and Evolution

2.1. Single Element Design

The proposed antenna undergoes a structured optimization process consisting of four well-defined stages to reach its final form, as illustrated in Figure 1. The initial step starts with a T-shaped radiating patch accompanied by a half-ground plane. This basic configuration serves as the foundation for further enhancements. In the second step, the T-shaped patch is strategically altered into an L-shaped structure, while maintaining the same half-ground plane. This transformation marks an essential phase in the design evolution, introducing changes that improve impedance matching and overall antenna performance.

In the third step, the radiating element is further developed into a U-shaped configuration, and the ground plane is extended to a full-size layout. However, this alteration, while structurally complete, introduces an impedance mismatch issue, likely due to increased surface currents on the expanded ground plane. This mismatch is evident

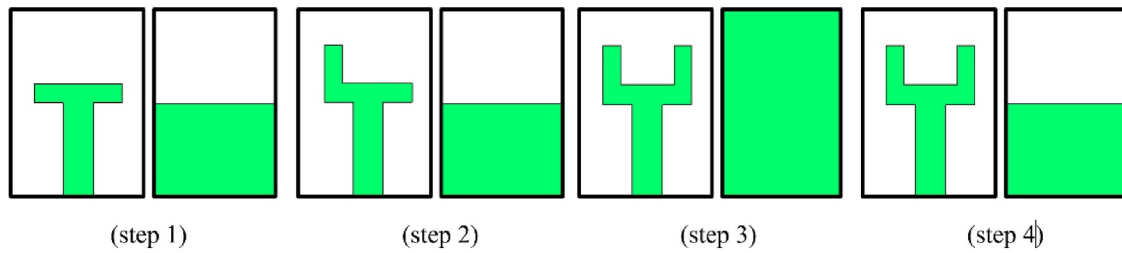


Figure 1. Optimization steps of the proposed antenna structure.

in the reflection coefficient response, signaling the need for further refinement. The fourth and final step addresses this issue by modifying the bottom ground plane into a DGS while keeping the U-shaped radiator intact. This adjustment proves to be pivotal in restoring impedance matching, reducing coupling effects, and improving the antenna's radiation characteristics. The final design successfully achieves wideband operation while maintaining compact geometry and efficient performance.

The reflection coefficient behavior across these design stages is demonstrated in Figure 2. In the initial configuration, the antenna maintains a reflection coefficient below -10 dB across 30–40 GHz, suggesting satisfactory impedance matching. With the L-shaped modification in step two, the bandwidth expands further, spanning 27.2–42 GHz, still with acceptable matching. However, in step three, the incorporation of a full ground plane leads to a deterioration in performance, as the reflection coefficient exceeds -10 dB, indicating a mismatch. This issue is corrected in the final step by modifying the ground plane, allowing the antenna to operate effectively across a significantly wider range from 22 to 46 GHz with consistent impedance matching. This broad operational bandwidth highlights the success of the iterative optimization process and establishes the antenna's suitability for 5G mm-Wave communications.

The physical structure of the final antenna is shown in Figure 3. It consists of a U-shaped radiating patch with a partially defected ground plane, designed to enhance bandwidth and suppress surface wave propagation. The antenna is fabricated on a high-performance, low-loss Rogers RT-Duroid 5880 substrate, which is widely used in high-frequency applications due to its favorable electrical properties. The substrate has a thickness of 0.8 mm, a dielectric constant (ϵ_r) of 2.2, and a low loss tangent of 0.0009, ensuring minimal dielectric losses during operation. The compact size of the substrate, measuring $10 \times 8 \times 0.8$ mm³, contributes to the antenna's suitability for integration in small 5G devices. The radiating patch is fed using a standard microstrip line to deliver maximum power efficiency to the antenna. The geometry and electromagnetic behavior of the proposed antenna are simulated and optimized using CST Microwave Studio. Table 1 summarizes the key dimensions and parameters of the finalized antenna design.

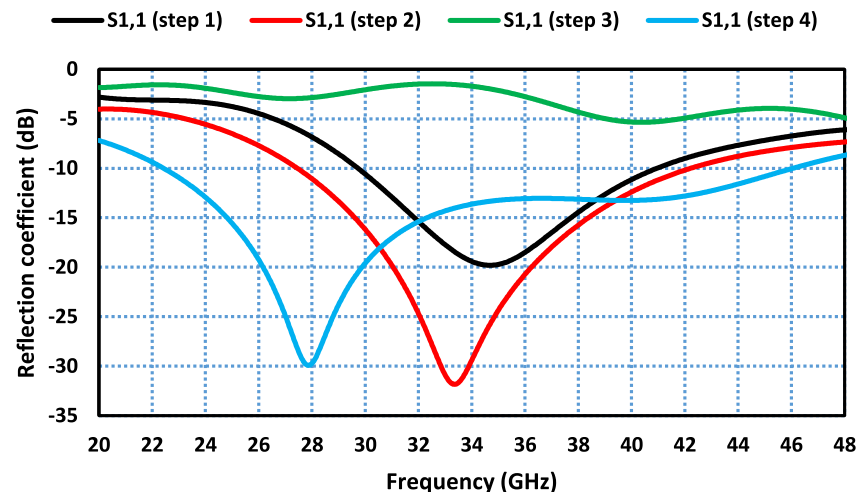


Figure 2. Reflection coefficient responses from the optimization steps carried out on the proposed antenna.

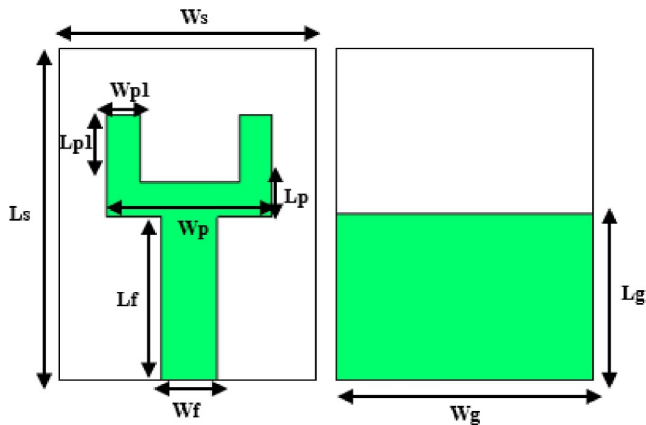


Figure 3. Geometry layout of the proposed antenna structure.

To further understand the influence of the ground plane on antenna performance, parametric study was conducted, and the results are presented in Figure 4. This analysis explores how variations in the ground plane length affect the reflection coefficient and, consequently, the antenna's bandwidth. The results reveal that a ground length of 5 mm provides the optimal reflection response, enabling stable and wide impedance bandwidth across 22–46 GHz. As the ground plane length deviates from this optimal value, either increasing or decreasing, the reflection coefficient becomes less favorable, leading to reduced bandwidth and degraded performance. These findings emphasize the critical role of precise ground plane design in achieving high-efficiency performance. Optimization of ground plane dimensions is, therefore, a vital step in ensuring the antenna's effectiveness across the desired mm-Wave frequency range.

2.2. Two-Element Antenna Array

Building upon the single-element antenna, a two-port antenna configuration is developed to improve overall system performance in terms of channel capacity, data throughput, and signal robustness. This two-element antenna structure is illustrated in Figure 5 and occupies compact dimensions of $10 \times 16 \times 0.8 \text{ mm}^3$. The expansion to a dual-element system marks a significant enhancement, enabling the antenna to exploit the advantages of spatial diversity while preserving a small footprint suitable for modern 5G device integration.

In this configuration, the two antenna elements are positioned orthogonally on the top surface of the substrate. This perpendicular orientation is a critical design strategy to maximize spatial diversity, which is essential for achieving low correlation between signals in multiport antenna systems. By aligning the elements at 90° to each other, the design enhances the ability to exploit multipath propagation, a phenomenon where transmitted signals travel through different paths due to reflection, scattering, and diffraction. This arrangement helps reduce the detrimental effects of signal fading, co-channel interference, and correlation, ultimately improving the reliability of the communication link.

The orthogonal placement also minimizes electromagnetic interaction between the elements, helping to maintain high isolation without the need for additional decoupling structures. As a result, each antenna element can operate independently, which is vital for channel decorrelation and signal integrity. Furthermore, this configuration contributes to the increase in channel capacity, enabling the system to support multiple data streams simultaneously, one of the key benefits of multiport antenna technology in high-speed wireless systems.

Despite its small size, the two-element antenna maintains strong electromagnetic performance. The compactness of the design is particularly important for applications in space-constrained environments such as smartphones, wearables, and other portable 5G devices. Careful attention has been paid to ensuring that size reduction does not compromise radiation efficiency or inter-element isolation.

The effectiveness of this multiport antenna configuration is validated through simulated S-parameter results, presented in Figure 6. The antenna exhibits an impressive impedance bandwidth ranging from 22 to 46 GHz, covering the entire Ka-band, which is extensively allocated for 5G millimeter-wave communications. Moreover, the system demonstrates excellent isolation levels greater than 20 dB across the operational frequency range. High isolation between the two radiating elements is critical for minimizing mutual coupling and ensuring that each port maintains its distinct transmission and reception characteristics.

Table 1
Design Parameters of the Proposed Antenna

Symbol	Dimensions (mm)
L_s	10
L_f	5
L_p	1
L_{p1}	2
L_g	5
L_{s1}	10
L_{g1}	10
L_{s2}	20
L_{g2}	20
L_m	25
W_s	8
w_f	1.7
W_p	5
W_{p1}	1
W_g	8
W_{s1}	16
W_{g1}	16
W_{s1}	26
W_{g2}	26
W_m	29

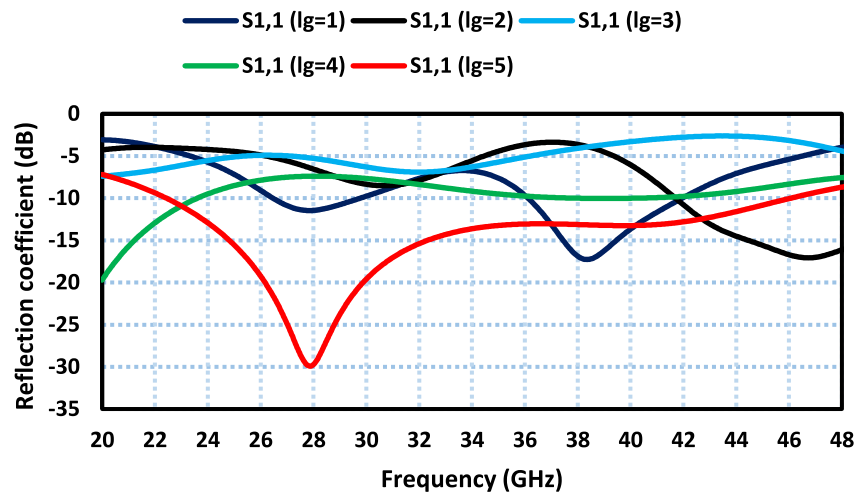


Figure 4. Effect of the ground plane on the proposed antenna.

This level of performance ensures that the proposed two-element antenna is capable of efficient signal management, making it highly suitable for modern 5G and beyond wireless systems that require robust communication across wide frequency bands. The combination of compact size, orthogonal arrangement, and strong isolation validates the design as a promising candidate for reliable, high-data-rate millimeter-wave applications.

2.3. Four-Element Antenna Configuration

The development of the proposed four-element antenna marks a significant step forward in the design of compact and high-performance antennas for 5G mm-Wave communication systems. This configuration is specifically designed to meet the increasing demands for higher channel capacity, support for elevated data traffic, and improved link reliability in dense and high-speed wireless environments.

As illustrated in Figure 7a, the antenna system comprises four radiating elements arranged in an orthogonal configuration on the top side of the substrate. Each element is carefully positioned perpendicularly to its adjacent counterparts, which is a deliberate spatial strategy to minimize mutual coupling. This orthogonal placement enhances isolation between ports, achieving values greater than 20 dB across the operational bandwidth. Remarkably, this high level of isolation is attained without the use of any additional decoupling structures, which helps maintain the simplicity and compactness of the design.

While the orthogonal placement of the four radiators establishes a baseline isolation, the intentional partial/disconnected ground configuration further limits surface-current continuity and suppresses near-field coupling paths. In other words, the orthogonal geometry reduces broadside coupling, and the engineered ground discontinuities attenuate substrate-supported and edge currents. The measured isolation >20 dB across 22–46 GHz is therefore the combined outcome of geometry and ground-plane engineering rather than either mechanism alone. This design choice is consistent with the single-element and two-element studies in Section 2.1 and 2.2 where ground tailoring improved matching and coupling behavior.

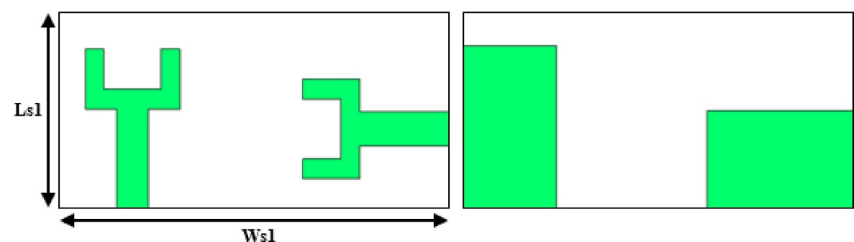


Figure 5. Front and back view of the proposed two element antenna array.

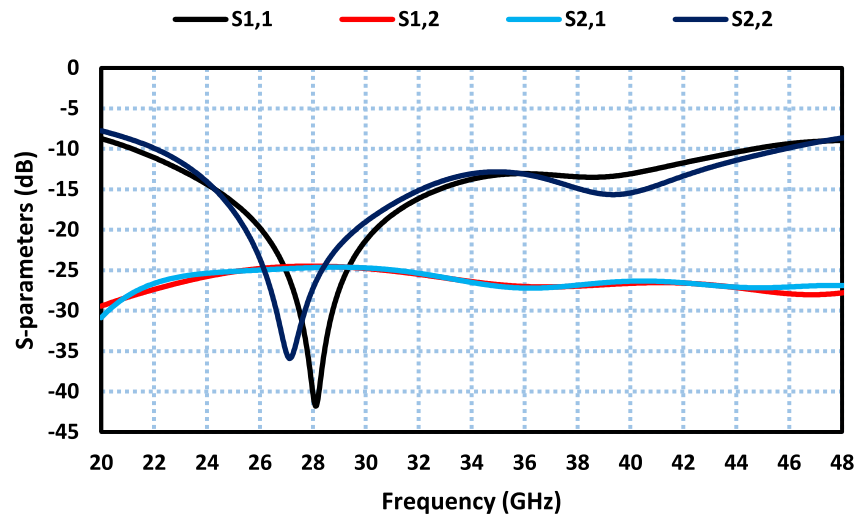


Figure 6. S-parameters of the proposed two-element antenna array.

Further contributing to the system's performance is the use of independent partial ground planes for each radiating element, as shown in the back view in Figure 7b. These ground planes are also arranged orthogonally and are isolated from one another, further reducing undesired surface currents and electromagnetic interference. This ground configuration supports the multiport antenna elements in operating independently and efficiently, reinforcing the system's overall radiation performance and stability.

The surface-current maps at 28 GHz (Figure 16) corroborate this mechanism by showing current confinement to the excited element with minimal spillover to orthogonal neighbors, consistent with both the orthogonal layout and the segmented ground strategy.

The physical dimensions of the full four-element antenna measure $20 \times 26 \times 0.8 \text{ mm}^3$, making it exceptionally compact and well-suited for integration into miniaturized 5G devices, such as smartphones, IoT modules, or wearable technology. The design is optimized to provide maximum functionality in environments where space is limited but performance cannot be compromised.

To evaluate the performance of this four-port system, S-parameter results are presented in Figure 8. The antenna exhibits a broad impedance bandwidth ranging from 22 to 46 GHz, covering the entirety of the Ka-band used in advanced 5G mm-Wave communications. Importantly, the isolation between all ports remains consistently above 20 dB across this entire frequency range, validating the effectiveness of the spatial and structural design.

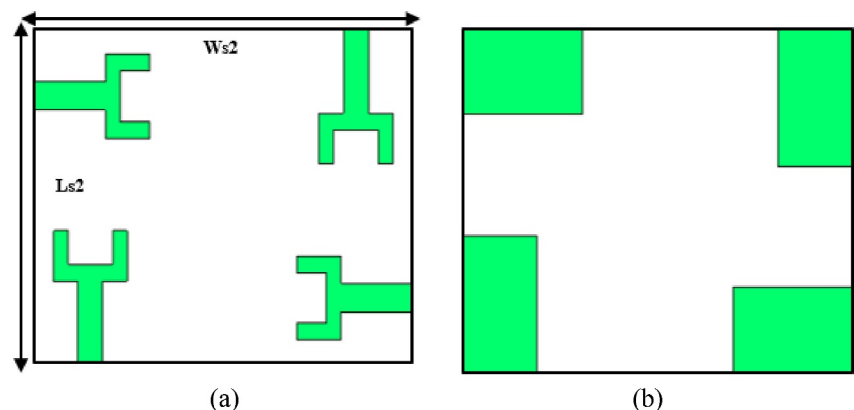


Figure 7. The proposed four-element antenna array, (a) front view, and (b) back view.

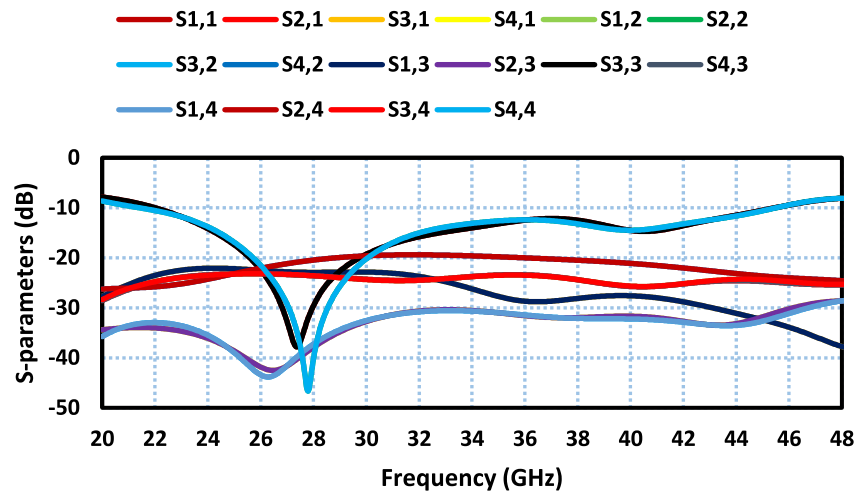


Figure 8. S-parameter response of the proposed multiport antenna array at each port.

High isolation and wide bandwidth are critical for effective multiport antenna operation, as they directly impact signal integrity, channel decorrelation, and the ability to transmit and receive multiple data streams simultaneously. The excellent S-parameter performance of the proposed four-element configuration confirms its ability to deliver robust and reliable wireless communication, with reduced interference and enhanced data handling capacity.

The proposed design successfully integrates multiple high-performing elements into a compact footprint, without sacrificing bandwidth or isolation. It stands out as a practical and efficient solution for next-generation wireless systems, offering high throughput, compactness, and strong multiport antenna capabilities suitable for a broad spectrum of 5G mm-Wave applications.

3. Frequency Selective Surface (FSS) Design and Integration

To enhance the gain and isolation performance of the proposed antenna system, a FSS layer is designed and optimized for mm-Wave applications. The unit cell that forms the basis of this FSS structure operates effectively over a wide frequency range from 24 to 44 GHz, making it well-suited for integration into 5G systems.

The FSS unit cell is fabricated on a Rogers RT-Duroid 5880 substrate, which is commonly used in high-frequency designs due to its excellent dielectric properties. The substrate has a thickness of 0.8 mm, a dielectric constant of 2.2, and a very low loss tangent, ensuring minimal energy loss during operation. The unit cell geometry, shown in Figure 9b, consists of two rectangular split-ring resonators arranged in an H-shaped configuration. The developmental stages of the unit cell are illustrated in Figure 9a. This resonator structure is simulated in the frequency domain using CSTMWS to evaluate its electromagnetic performance.

The effectiveness of the unit cell design is validated through the reflection coefficient plot shown in Figure 9c. The reflection coefficient remains within acceptable limits across the 24–44 GHz band, confirming that the unit cell exhibits strong band-pass filtering characteristics. Additionally, the transmission coefficient curve demonstrates minimal signal loss across this range, indicating high transmission efficiency, a critical factor for maintaining signal strength and quality in multiport antenna systems.

Following the successful validation of the unit cell, a complete FSS surface is constructed by arranging a periodic array of 6×7 unit cells with a small spacing gap (denoted as “g”) between adjacent elements. The overall dimensions of the FSS surface are defined by $L_m \times W_m$, as shown in Figure 10a. This periodic array creates a spatially varying electromagnetic response that enables frequency-selective behavior, allowing specific frequencies to pass while suppressing others.

The FSS layer is positioned above the multiport antenna at a specific height ‘H’, as illustrated in Figure 10b. This strategic placement plays a pivotal role in enhancing the radiation characteristics of the antenna system. The FSS acts as an electromagnetic filter, selectively transmitting desired frequencies while attenuating unwanted

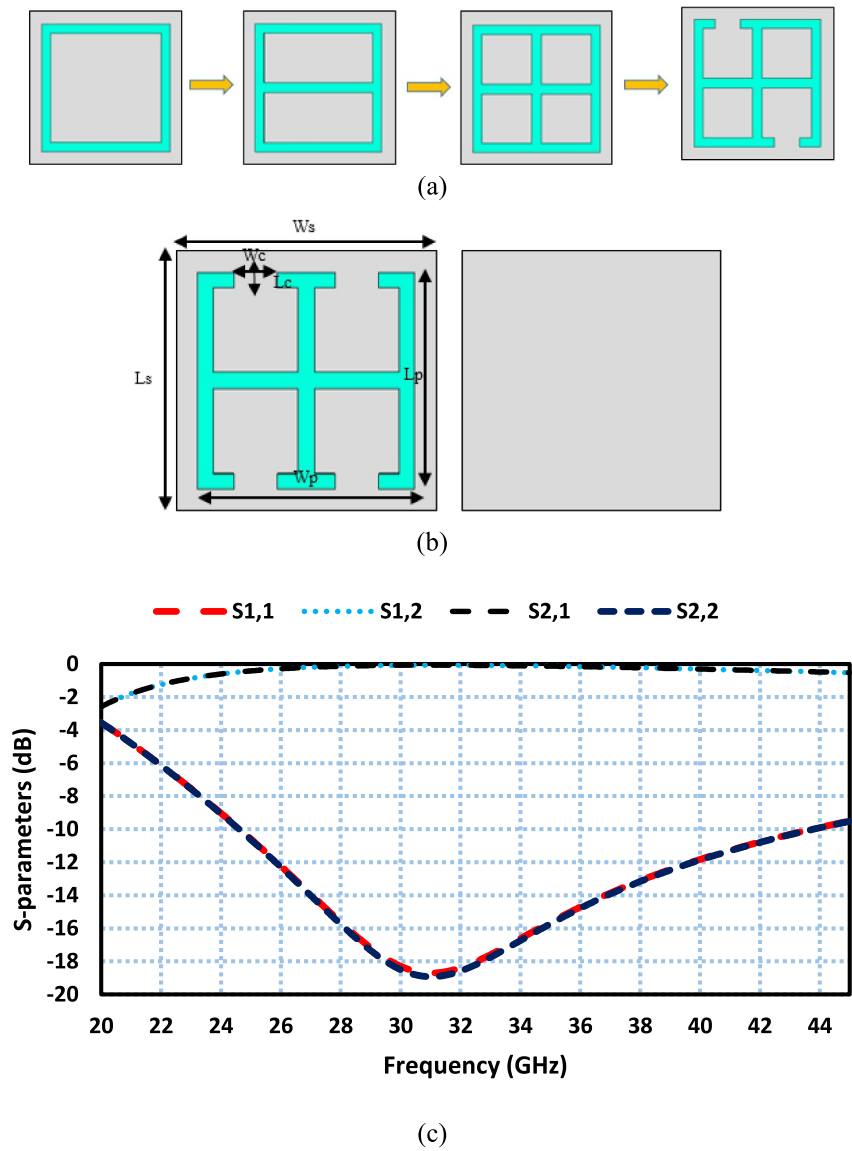


Figure 9. (a) Steps to create the unit cells, (b) final unit cell geometry, and (c) S-parameters of the unit cell.

components and reducing interference. This results in improved signal clarity, reduced mutual coupling, and enhanced gain across the operating band.

The reflection and transmission performance of the multiport antenna with and without the FSS layer are compared in Figure 10c. While the reflection coefficient remains relatively unchanged, with the impedance bandwidth maintained from 22 to 46 GHz, the transmission coefficient improves slightly, increasing from 19 to 21 dB. This demonstrates a moderate but valuable improvement in inter-element isolation, indicating that the FSS contributes positively to overall system performance without altering the matching characteristics.

The optimal placement height between the multiport antenna and the FSS layer is determined based on the following phase condition (Din et al., 2022):

$$\phi_{FS}(S) - 2\beta H = 2n\pi \quad \text{where, } n = \dots -1, 0, 1 \dots \quad (1)$$

In this equation, ϕ_{FSS} represents the phase of the reflected wave from the FSS, β is the propagation constant in free space, and H is the vertical separation between the multiport antenna array and the FSS layer. To achieve optimal

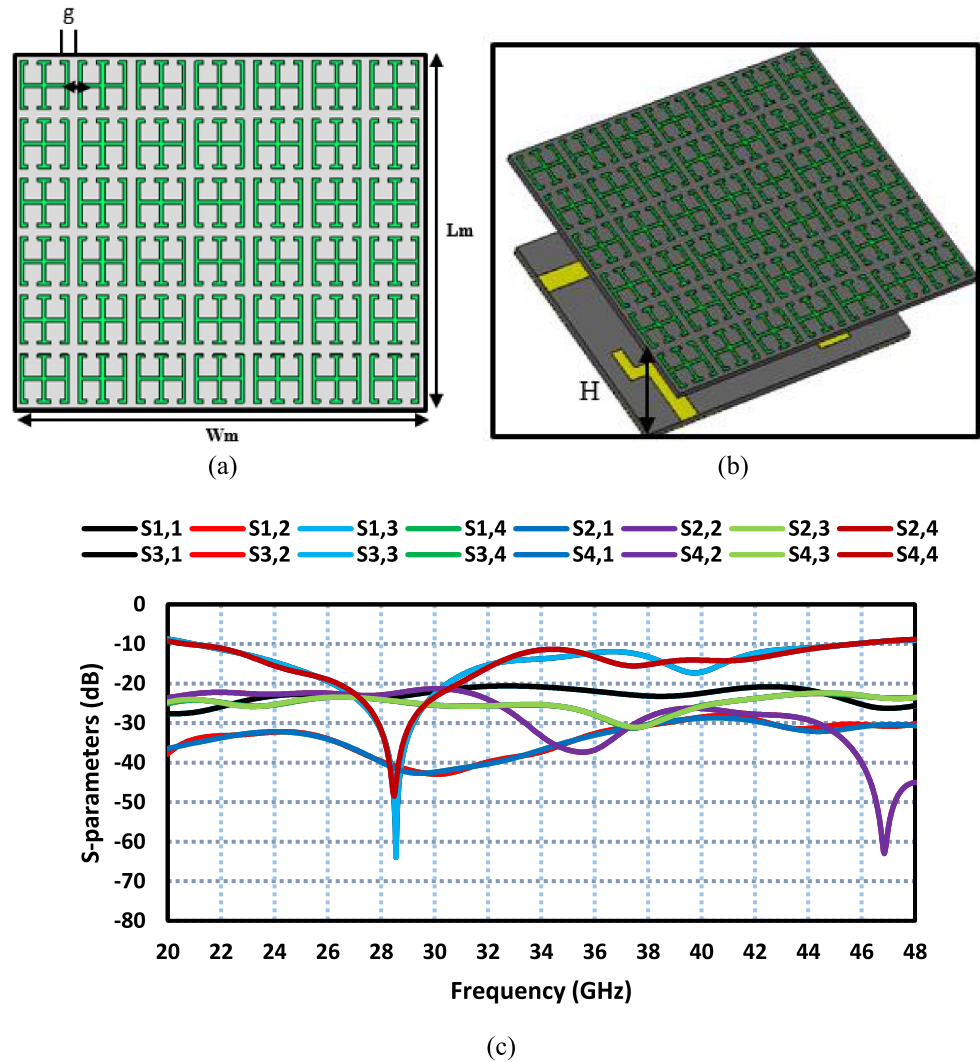


Figure 10. (a) 6×7 antenna array, (b) proposed frequency selective surface (FSS) based 6×7 antenna array, and (c) S-parameters of the proposed FSS based 6×7 antenna array.

constructive interference and maximize gain, the height H must correspond to an integer multiple of half the wavelength at the design frequency. However, because the FSS is intended to operate over a wide bandwidth, fine-tuning of this height is essential for maximizing overall system gain and performance.

To determine the optimal value of H , a parametric analysis is performed using different height values between the FSS and the multiport antenna structure. As shown in Figure 11, a height of 5 mm results in a gain of 6.7 dBi. When the height is increased to 7.5 mm, the gain reaches its maximum value of 7.5 dBi. However, increasing the height further to 10 mm leads to a reduction in gain to 7 dB, indicating that the optimal constructive interference condition is no longer satisfied.

From this analysis, it is concluded that the optimal height for placing the FSS above the multiport antenna is 7.5 mm. At this height, the multiport antenna achieves its peak gain while preserving wide bandwidth and high efficiency. The final optimized configuration, therefore, consists of a 6×7 FSS layer stacked 7.5 mm above the four-element antenna. This configuration effectively enhances radiation characteristics and system performance across the entire 5G mm-Wave frequency band.

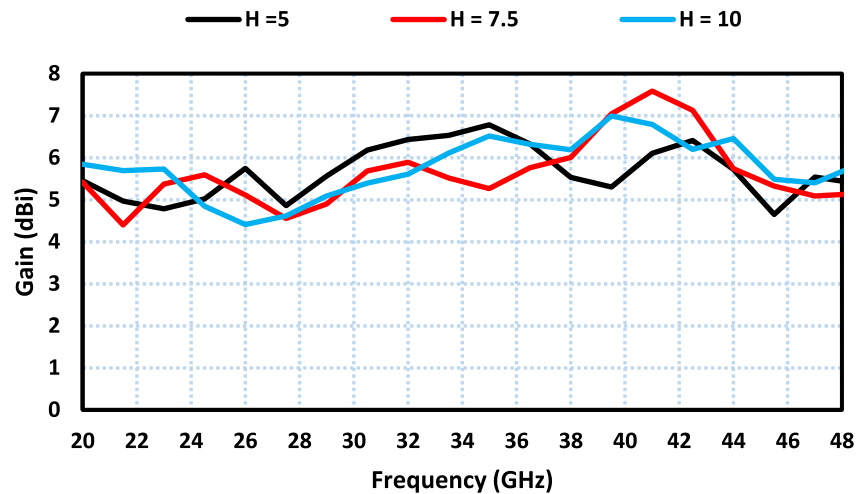


Figure 11. Simulated gain at different gap heights between the frequency selective surface and multiport antenna array.

4. Simulated and Measured Performance

To validate the simulated performance of the proposed multiport antenna enhanced with FSS, a physical prototype was fabricated, as shown in Figure 12. In this implementation, a lightweight foam spacer is used to support the FSS layer above the multiport antenna. The foam ensures a stable and precise vertical separation between the FSS and the radiating elements, maintaining the optimal spacing of 7.5 mm identified through simulation.

The connector and feed transition were not modeled in the EM simulations to maintain generality of the design. In measurements, precision 2.92 mm connectors and phase-stable cables were used, and the VNA was calibrated up to the connector reference plane. Connector repeatability and insertion loss were included in the uncertainty budget, contributing less than 0.2 dB variation to the measured gain and efficiency.

A comparative analysis between the simulated and measured results was conducted to assess the real-world applicability and accuracy of the design. This comparison plays a crucial role in validating the performance, efficiency, and isolation characteristics of the fabricated multiport antenna.

The S-parameters of the fabricated system are presented in Figure 13, offering a detailed view of both reflection and transmission characteristics. Figure 13a shows the anechoic-chamber configuration used for all measurements. The proposed antenna was mounted on a low-scattering foam column atop a dual-axis positioner (azimuth–elevation). The transmit antenna was a standard-gain horn covering the band of interest, used as the reference antenna for absolute gain calibration. The chamber walls, floor, and ceiling were fully lined with pyramidal absorbers to maintain a quiet zone around the antenna under test. Chamber conditions were controlled at

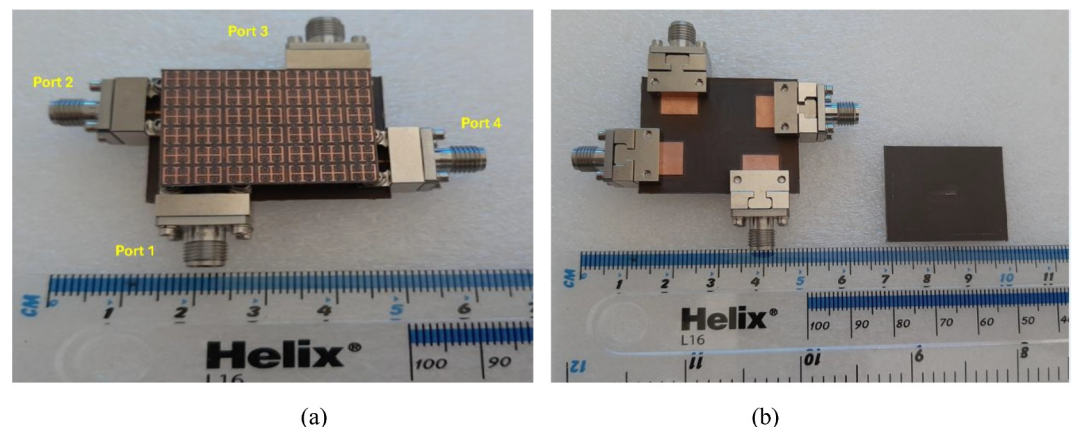


Figure 12. Fabricated frequency selective surface-based multiport antenna, (a) front view, and (b) back view.

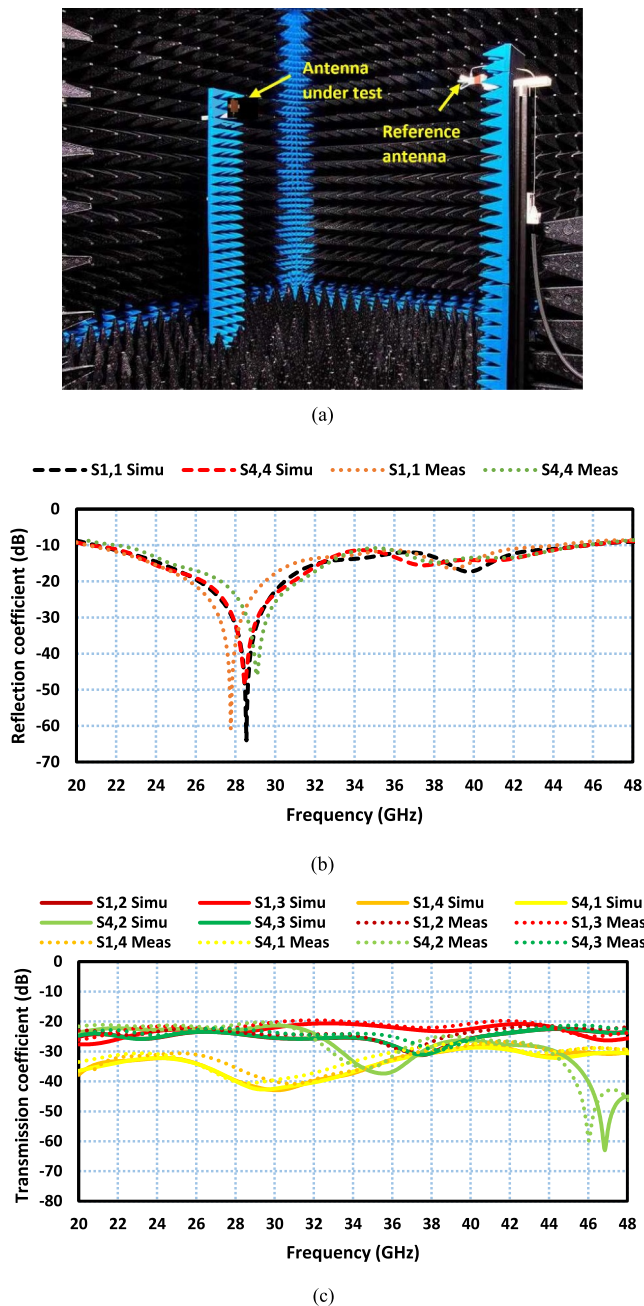


Figure 13. The proposed frequency selective surface-based multiport antenna's simulated and measured performance, (a) measurement setup, (b) reflection coefficient response, and (c) transmission coefficient response.

values over 22–46 GHz. The uncertainty budget combines: VNA magnitude/phase residuals and calibration standards, cable/connector repeatability and drift, chamber probe factor and quiet-zone ripple, AUT alignment/positioning, reference-antenna gain (when applicable), near-to-far-field processing, and mismatch corrections. We report the expanded uncertainty (U) with a coverage factor of $k \approx 2$, corresponding to a 95% confidence level, for the measured gain (7.5 dBi) and total efficiency (93%). Measurements were performed in an anechoic chamber at $T = 23 \pm 2^\circ\text{C}$, relative humidity $\text{RH} = 45 \pm 5\%$.

The surface current distribution at 28 GHz is analyzed in Figure 16 to understand the electromagnetic interaction between ports. When a single port (e.g., Antenna 1) is excited while the others are terminated with matched loads, the current is largely confined to the excited element. Due to the orthogonal placement of the multiport antenna

$T = 23 \pm 2^\circ\text{C}$ and $\text{RH} = 45 \pm 5\%$. A vector network analyzer was used with waveguide/coax extenders appropriate to the band. A full calibration was performed at the chamber feed reference plane before each measurement run. The separation between the reference antenna and the proposed antenna was set to satisfy the far-field condition. Figure 13b displays the measured and simulated reflection coefficients for Antennas 1 and 4 across the 22–46 GHz range, confirming a wide impedance bandwidth of 24 GHz. Figure 13c illustrates the transmission coefficients (S-parameters) between Antennas 1 and 4, and between Antennas 2 and 3, capturing the inter-element isolation within the multiport antenna. The results reveal that the minimum measured isolation is around 20 dB, while the maximum reaches up to 39 dB, highlighting the antenna's strong capability to mitigate mutual coupling and interference across the entire operating band.

While some minor discrepancies between the measured and simulated results are observed, these can be attributed to fabrication imperfections, connector and cable losses, and measurement calibration errors. Nevertheless, the overall trends and values show close agreement, validating the reliability of the simulation approach and the design's effectiveness in real-world scenarios.

Further performance evaluation was conducted through radiation pattern measurements in an anechoic chamber, ensuring minimal reflection and external interference. The measured and simulated radiation patterns for both the H-plane and E-plane at 28 and 37 GHz are illustrated in Figures 14a and 14b. In the H-plane, the main radiation lobe is concentrated within the angular range of 90° – 150° , indicating strong directivity and focused radiation. Conversely, the E-plane patterns reveal broader radiation coverage, with the main lobe spanning -150° – 150° , which is beneficial for applications requiring coverage over wider elevation angles. These patterns demonstrate that the antenna delivers both focused and broad radiation characteristics depending on the plane, enabling versatility in different communication environments.

The system's gain and efficiency performance are also verified. Figure 15a shows that the peak gain of the antenna reaches 7.5 dBi at 41 GHz, correlating with improved radiation directivity at higher frequencies. As shown in Figure 15b, the total efficiency peaks at 93% at 30 GHz, with values consistently above 80% across the full 22–46 GHz operating range. These results strongly align with the simulated predictions, reinforcing the accuracy of the design and modeling techniques employed.

We performed independent mount-measure cycles with fresh VNA calibrations for each run. At 41 GHz, the peak gain across five measurement runs is mean \pm standard deviation (SD) with a 95% confidence interval (CI); at 30 GHz (efficiency maximum), the total efficiency is likewise reported as mean \pm SD (95% CI) and we also provide band-averaged

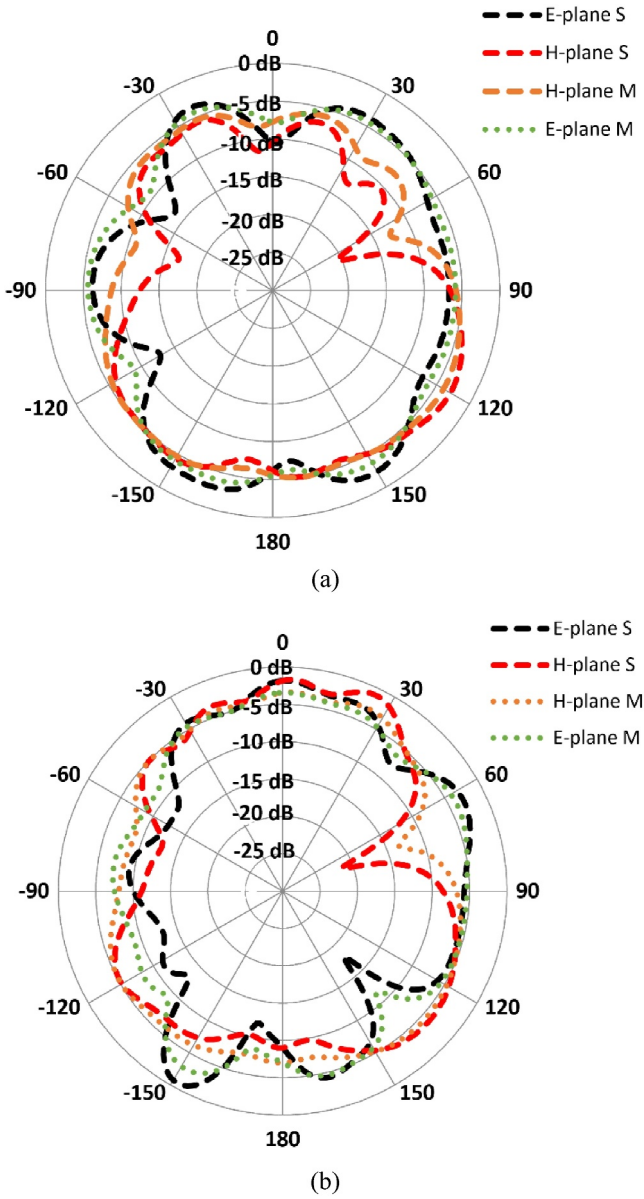


Figure 14. Simulated (S) and measured (M) E-plane and H-plane radiation patterns of the proposed frequency selective surface-based multiport antenna, (a) at 28 GHz, and (b) at 37 GHz.

elements, minimal coupling is observed with Antennas 3 and 4, confirming the effectiveness of spatial separation. Additionally, the presence of the FSS layer above the radiating elements influences current flow, as energy is partially distributed across the unit cells of the FSS. This distributes surface currents, helping further suppress mutual coupling and enhancing overall system performance.

The measured results closely align with simulations across all key parameters namely impedance bandwidth, isolation, gain, efficiency, and radiation characteristics. These findings demonstrate the robustness of the proposed multiport antenna design and validate its potential for use in practical 5G mm-Wave communication systems.

5. Multiport Antenna Performance Evaluation

To evaluate the effectiveness of the proposed multiport antenna, several key performance metrics are analyzed. These parameters are essential in assessing the system's ability to maintain signal integrity, reduce inter-element interference, and support reliable high-capacity wireless communication. Among the most critical indicators are the Envelope Correlation Coefficient (ECC) and Diversity Gain (DG).

5.1. Envelope Correlation Coefficient (ECC)

ECC is a crucial metric in multiport antenna system evaluation. It quantifies the degree of correlation between signals received or transmitted by different antenna elements. An ECC value close to zero indicates that the signals are largely uncorrelated, which is desirable for ensuring high data throughput and reliable performance in multipath environments.

For the proposed four-element FSS-based multiport antenna, the ECC was computed using far-field radiation pattern data, which provides a more accurate representation of real-world antenna behavior over a wide frequency range. The ECC is mathematically defined by:

$$ECC = \frac{|\iint 4\pi (M_i(\theta, \phi)) \times (M_j(\theta, \phi)) d\Omega|^2}{\iint 4\pi |M_i(\theta, \phi)|^2 d\Omega \iint 4\pi |M_j(\theta, \phi)|^2 d\Omega} \quad (2)$$

Where:

- $M_i(\theta, \phi)$ and $M_j(\theta, \phi)$ are the complex radiation patterns of antenna elements i and j , respectively,
- $d\Omega$ denotes the differential solid angle over a 3D sphere.

As illustrated in Figure 17, the ECC values for the proposed multiport antenna are consistently below 0.005 across the entire operating band. This value is well below the industry-accepted threshold of 0.5, indicating excellent isolation and minimal correlation among the antenna elements. Such low ECC ensures effective multipath signal exploitation and significantly enhances overall system capacity and performance in real-world scenarios (Kildal & Rosengren, 2004).

5.2. Diversity Gain (DG)

Diversity Gain is another important parameter in multiport antenna systems, representing the improvement in signal quality due to the presence of multiple uncorrelated transmission paths. A higher DG reflects better resilience to fading and more reliable data transmission.

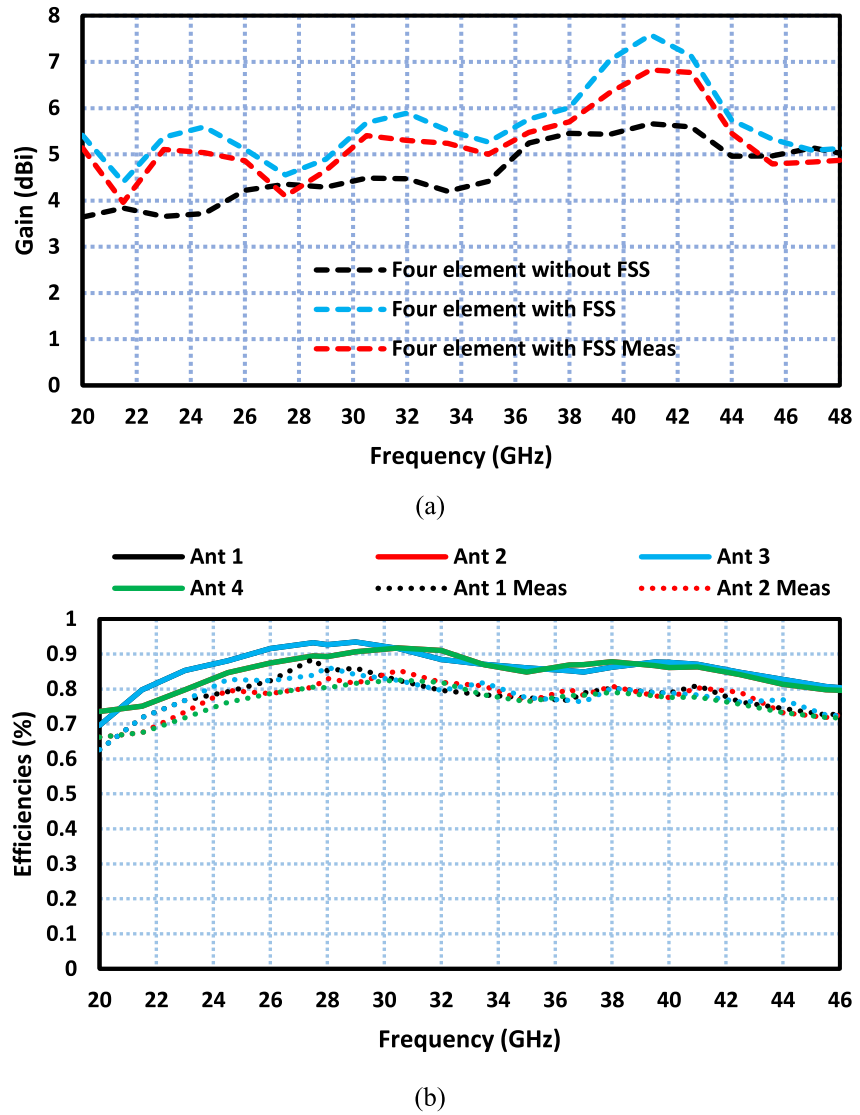


Figure 15. Simulated and measured of the proposed frequency selective surface based multiport antenna, (a) Antenna gain, and (b) total radiation efficiency.

DG is derived directly from ECC using the following expression:

$$DG = 10\sqrt{1 - |ECC|^2} \quad (3)$$

As shown in Figure 17, the DG for the proposed multiport antenna is approximately 10 dB across the entire 22–46 GHz frequency range, which is considered ideal. This consistent high DG further confirms that the antenna system performs robustly under fading channel conditions and provides enhanced link reliability (Li et al., 2012).

Channel capacity loss quantifies the reduction in link capacity caused by inter-element correlation and mismatch. Figure 18 shows that Channel capacity loss < 0.4 bit/s/Hz across 20–48 GHz, meeting the commonly accepted practical criterion. Total active reflection coefficient (TARC) evaluates the aggregate mismatch under multiport excitation; for practical systems a target of $TARC \leq -10$ dB is typically used. Figure 18 confirms the average TARC remains below -10 dB over 20–48 GHz. Together, these metrics indicate that the proposed FSS-based multiport antenna provides strong spatial diversity, high inter-element isolation, and robust multipath resilience, making it well-suited for next-generation 5G mm-wave systems.

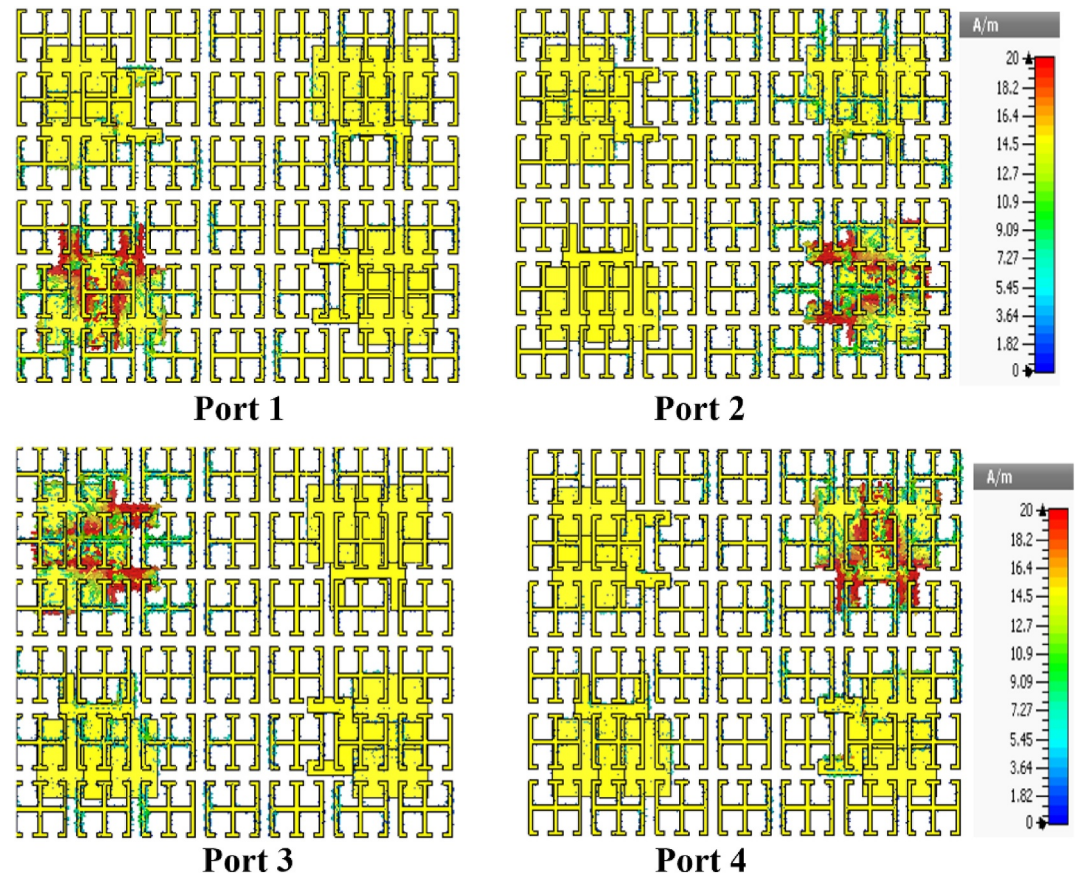


Figure 16. Surface current distribution at 28 GHz across each port of the proposed frequency selective surface based multiport antenna array.

5.3. Statistical Validation of Multiport Antenna Metrics

We performed $N = 5$ independent mount-measure cycles under identical chamber conditions. For each run, ECC (pattern-based) and DG were computed across the 22–46 GHz band. We report mean \pm SD and 95% confidence intervals (CI) for band-averaged ECC and DG, and at the representative frequency of 28 GHz. A paired t -test

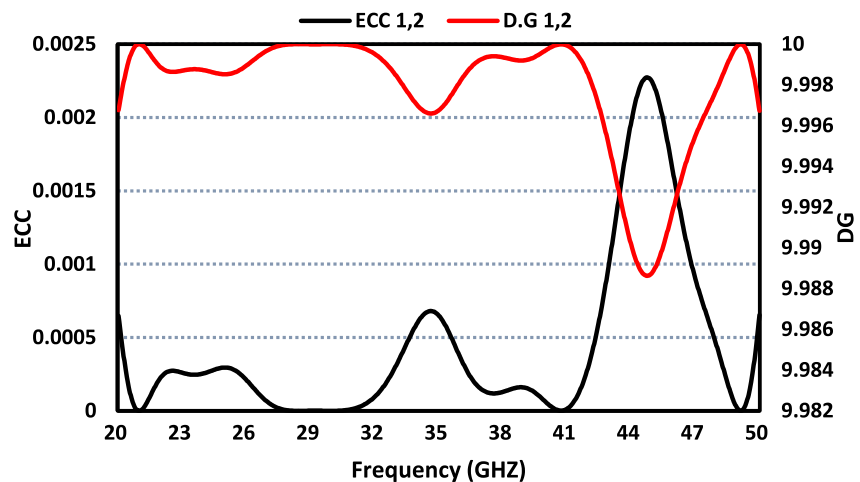


Figure 17. Envelope correlation coefficient and diversity gain of the proposed frequency selective surface-based multiport antenna array.

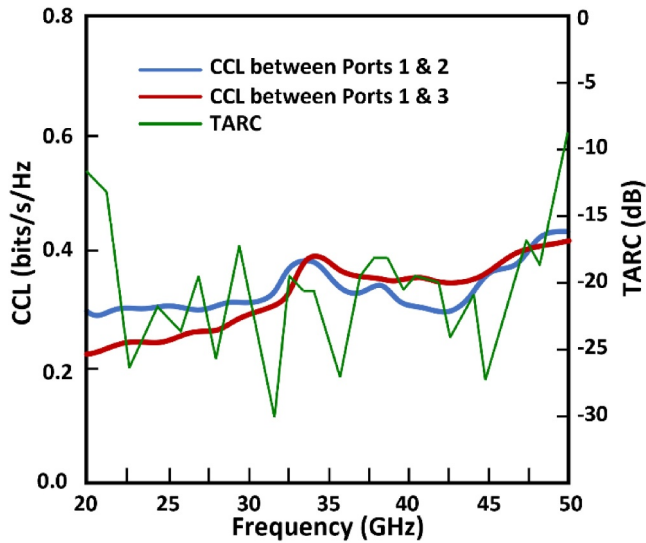


Figure 18. CLL and total active reflection coefficient of the proposed frequency selective surface-based multiport antenna array.

between measured and simulated values shows no significant difference at the 95% confidence level ($p > 0.05$). A one-way ANOVA across repeated runs indicates no significant inter-run variation for either metric ($p > 0.05$). These results demonstrate that the observed low ECC and ≈ 10 dB DG are statistically reliable and repeatable.

6. Comparative Analysis With Recent Literature

To evaluate the performance of the proposed mm-Wave multiport antenna system, a comparative analysis has been conducted against several recently reported designs as shown in Table 2. Key parameters such as antenna size, frequency range, decoupling technique, isolation, radiation efficiency, and ECC were used to benchmark the proposed antenna's capabilities.

The design reported in (Gao et al., 2020) employs a printed patch structure operating in the 5–10 GHz band with a dielectric block for decoupling. It achieves 20.6 dB isolation and 97% radiation efficiency; however, it does not extend into the millimeter-wave spectrum required for 5G applications, and no ECC values are provided.

In Zhang et al. (2019), a DRADRA array operating in the 26–30 GHz range uses metal strips to enhance isolation. It achieves 24 dB isolation and an ECC of 0.013, but radiation-efficiency data are unavailable, and its bandwidth is narrower than that of the proposed design.

A wideband printed patch antenna presented in Sehrai et al. (2020) covers 20–40 GHz without employing any specific decoupling mechanism. It provides 20 dB isolation, 70% efficiency, and an ECC of 0.0014; however, its large physical footprint ($80 \times 80 \times 1.57 \text{ mm}^3$) limits its suitability for compact 5G devices.

In Tariq et al. (2021), a metasurface-based printed patch designed for 24–27 GHz achieves very high isolation (45 dB) and an exceptionally low ECC of 1×10^{-7} , though it offers limited bandwidth and lacks radiation-efficiency data, restricting its applicability to wideband 5G systems.

The antenna in Munir et al. (2023) employs a DGS to achieve 20 dB isolation across 23–41 GHz, with 82% radiation efficiency and a very low ECC of 0.00015. The proposed antenna, however, surpasses it in both frequency coverage and efficiency.

Table 2
Performance Comparison of the Proposed mm-Wave Multiport Antenna With Recent Literature

References	Antenna size (mm^2)	Type of antenna	Frequency range (GHz)	Decoupling method	Isolation (dB)	Radiation efficiency (%)	ECC
Gao et al. (2020)	—	Printed patch	5–10	Dielectric Block	20.6	97	—
Zhang et al. (2019)	20×20	DRA	26–30	Metal strips	24	—	0.013
Sehrai et al. (2020)	$80 \times 80 \times 1.57$	Printed patch	20–40	—	20	70	0.0014
Tariq et al. (2021)	30×43	Printed patch	24–27	Metasurface	45	—	0.1×10^{-6}
Munir et al. (2023)	48×12	Printed patch	23–41	Defected ground structure	20	82	0.00015
Abbas et al. (2023)	33×33	Printed patch	20–50	Orientation and Defected ground structure	—	80	0.005
Alqwaify et al. (2025)	$40 \times 85 \times 1.52$	Printed patch	22–28	Gap spacing	35	98	0.16
Awan et al. (2025)	30×30	Printed patch	22.5–29.8	Orientation	23	96	0.2
Bilal et al. (2022)	30×35	Printed patch	27.5–28.5	Orientation and FSS	40	83	0.0003
Proposed work	25×29	Printed patch	22–46	Metasurface and DGS	20	93	0.0005

Reference (Abbas et al., 2023) introduces a compact four-port printed antenna with orthogonal orientation and DGS-based decoupling. Although the isolation is not explicitly stated, it achieves 80% efficiency and an ECC of 0.005. The proposed design demonstrates superior efficiency (93%) and lower correlation (ECC = 0.0005).

Additional recent studies further highlight progress in wideband mm-Wave multiport antenna design. In Alqwaify et al. (2025), a gap-spaced four-port printed patch operating from 22 to 28 GHz achieves 35 dB isolation and 98% efficiency but over a narrower bandwidth. The design in Awan et al. (2025) covers 22.5–29.8 GHz with 23 dB isolation and 96% efficiency using orientation-based decoupling. A metasurface-assisted configuration in Bilal et al. (2022) achieves 40 dB isolation and an extremely low ECC of 0.0003 near 28 GHz, though it operates over a single narrow band. Compared to these, the proposed antenna offers a substantially wider operating range (22–46 GHz) while maintaining 20 dB isolation and 93% efficiency.

Overall, the proposed multiport antenna combines metasurface loading and a DGS to realize a compact ($25 \times 29 \text{ mm}^2$), wideband (22–46 GHz), and high-efficiency (93%) solution. With 20 dB isolation and ECC = 0.0005, it demonstrates excellent inter-element decoupling, minimal correlation, and suitability for next-generation 5G mm-Wave communication systems.

7. Conclusion

This paper presented a novel four-element wideband multiport antenna system integrated with a 6×7 frequency-selective surface (FSS) for 5G mm-wave applications. Operating across an ultra-wide 22–46 GHz band, the prototype achieves isolation >20 dB, peak realized gain of 7.5 dBi, and maximum total efficiency of 93% within a compact $25 \times 29 \times 0.8 \text{ mm}^3$ footprint. A perpendicular (orthogonal) arrangement of radiators together with an engineered DGS suppresses mutual coupling without resorting to bulky decoupling networks, preserving simplicity and manufacturability.

The key innovation lies in the precisely optimized FSS superstrate, positioned at a height selected to satisfy a constructive-interference phase condition over the band. This integration enhances directivity and realized gain while maintaining low correlation among ports. The design methodology, from a single radiator to a four-port configuration, demonstrates a scalable, stepwise approach that can be extended to denser arrays and module-level integration.

Comprehensive measurements substantiate the results. The MIMO-style performance metrics for multiport systems show ECC <0.0005 and DG ≈ 10 dB, confirming high diversity potential and minimal inter-element correlation across the full Ka-band. Statistical validation based on $N = 5$ independent mount-measure cycles reports mean \pm SD and 95% confidence intervals, and a measurement uncertainty budget (expanded uncertainty U , $k \approx 2$) was compiled to quantify instrumentation, cabling, chamber, alignment, and connector contributions. These steps, coupled with calibration to the connector reference plane, establish strong simulation-measurement agreement and experimental reliability.

From an implementation perspective, the use of standard low-loss substrates, foam spacing for the FSS, and a small form factor supports straightforward embedding in 5G modules, handsets, and IoT devices where throughput, isolation, and efficiency are simultaneously critical. The ability to maintain >80% efficiency across 22–46 GHz while holding isolation above 20 dB positions the design as a robust, wideband front-end for next-generation mm-wave links.

Future work will investigate: (a) reconfigurable or programmable FSS layers to enable dynamic beam shaping and band tailoring; (b) on-package/on-board integration with RF front-ends to assess co-design benefits and thermal/assembly tolerances; (c) array scaling and beamforming, leveraging the orthogonal/DGS foundation; and (d) full 3D far-field visualization and OTA throughput testing under channel emulation to complement the 2D pattern set reported here.

The proposed FSS-enhanced multiport antenna delivers a compact, efficient, and genuinely wideband solution for 5G mm-wave systems, uniting high isolation, enhanced gain, and ultra-low correlation under a rigorously validated measurement framework. These attributes mark a distinct advancement over current state-of-the-art designs and provide a practical platform for high-throughput, low-interference wireless applications.

Conflict of Interest

The authors declare no conflicts of interest relevant to this study.

Data Availability Statement

Data were not used, nor created for this research.

Acknowledgments

Co-funded by the European Union. Views and opinions expressed are however those of the author(s) only and do not necessarily reflect those of the European Union or the European Research Executive Agency. Neither the European Union nor the granting authority can be held responsible for them. Besides that, this publication has emanated from research jointly funded by Taighde Éireann-Research Ireland under Grant 13/RC/2094_2, the European Union's Marie Skłodowska-Curie Actions under Grant 101126578 and was supported in part by University of Galway. Additionally the authors appreciate the Princess Nourah bint Abdulrahman University Researchers Supporting Project number (PNURSP2025R828), Princess Nourah bint Abdulrahman University, Riyadh, Saudi Arabia.

References

- Abbas, M. A., Allam, A., Gaafar, A., Elhennawy, H. M., & Sree, M. F. A. (2023). Compact UWB MIMO antenna for 5G millimeter-wave applications. *Sensors*, 23(5), 2702. <https://doi.org/10.3390/s23052702>
- Alqwaifi, N. A., Awan, W. A., Alsaab, N., Alsunaydi, F. N., & Alhassoon, K. (2025). Array-inspired wideband and high-gain antenna with enhanced pattern diversity for 5G mm-wave networks. *Scientific Reports*, 15(1), 27383. <https://doi.org/10.1038/s41598-025-12868-w>
- Altakhaineh, A. T., Alja'afreh, S. S., Almatarneh, A. M., Almajali, E., Al-Tarawneh, L., & Yousaf, J. (2023). A quad-band shared-aperture antenna based on dual-mode/QMSIW cavity resonators. *Electronics*, 12(11), 2480. <https://doi.org/10.3390/electronics12112480>
- Awan, W. A., Abbas, A., Choi, D., Hussain, N., Lee, H., Sim, D., & Kim, N. (2025). Compact and directional dual-band antenna with low mutual coupling MIMO configuration for mm-wave communication. *Results in Engineering*, 26, 105457. <https://doi.org/10.1016/j.rineng.2025.105457>
- Bao, L., Fu, X., Wu, R. Y., Ma, Q., & Cui, T. J. (2022). Full-space manipulations of electromagnetic wavefronts at two frequencies by encoding both amplitude and phase of metasurface. *Advanced Materials Technologies*, 6(4), 2001032. <https://doi.org/10.1002/admt.202001032>
- Bilal, M., Naqvi, S. I., Hussain, N., Amin, Y., & Kim, N. (2022). High-isolation MIMO antenna for 5G millimeter-wave communication systems. *Electronics*, 11(6), 962. <https://doi.org/10.3390/electronics11060962>
- Desai, A., Upadhyaya, T., & Patel, R. (2019). Compact wideband transparent antenna for 5G communication systems. *Microwave and Optical Technology Letters*, 61(3), 781–786. <https://doi.org/10.1002/mop.31601>
- Din, I. U., Ullah, S., Naqvi, S. I., Ullah, R., Ullah, S., Ali, E. M., & Alibakhshikenari, M. (2022). Improvement in the gain of UWB antenna for GPR applications by using frequency-selective surface. *International Journal of Antennas and Propagation*, 2022, 1–12. <https://doi.org/10.1155/2022/2002552>
- Dokmetas, B., Arican, G. O., & Yilmaz, B. A. (2024). A folded pyramid-shaped microstrip antenna with improved bandwidth. In *2024 IEEE international symposium on antennas and propagation and INC/USNC-URSI radio science meeting (AP-S/INC-USNC-URSI)*, Firenze, Italy (pp. 1273–1274).
- Gao, D., Cao, Z. X., Fu, S. D., Quan, X., & Chen, P. (2020). A novel slotarray defected ground structure for decoupling microstrip antenna array. *IEEE Transactions on Antennas and Propagation*, 68(10), 7027–7038. <https://doi.org/10.1109/tap.2020.2992881>
- Hasan, M. M., Islam, M. T., Alam, T., Kirawanich, P., Alamri, S., & Alshammari, A. S. (2024). Metamaterial-loaded miniaturized extendable MIMO antenna with enhanced bandwidth, gain and isolation for 5G sub-6 GHz wireless communication systems. *Ain Shams Engineering Journal*, 15(12), 103058. <https://doi.org/10.1016/j.asej.2024.103058>
- Hong, W. (2017). Solving the 5G mobile antenna puzzle: Assessing future directions for the 5G mobile antenna paradigm shift. *IEEE Microwave Magazine*, 18(7), 86–102. <https://doi.org/10.1109/mmm.2017.2740538>
- Hussain, Q., Abbas Awan, W., Abu Sufian, M., Choi, D., Hussain, N., Gil, S. K., & Kim, N. (2024). Conformal millimeter-wave non-uniform dipole array with improved gain and bandwidth. *IEEE Access*, 12, 113036–113048. <https://doi.org/10.1109/access.2024.3443075>
- Iskandarani, M. Z. (2024). Investigation of energy consumption in WSNs within enclosed spaces using beamforming and LMS (BF-LMS). *IEEE Access*, 12, 63932–63941. <https://doi.org/10.1109/access.2024.3395932>
- Jang, T. H., Kim, H. Y., Kang, D. M., Kim, S. H., & Park, C. S. (2019). 60 GHz low-profile, wideband dual-polarized U-slot coupled patch antenna with high isolation. *IEEE Transactions on Antennas and Propagation*, 67(7), 4453–4462. <https://doi.org/10.1109/tap.2019.2911623>
- Jilani, S. F., & Alomainy, A. (2018). Millimetre-wave T-shaped MIMO antenna with defected ground structures for 5G cellular networks. *IET Microwaves, Antennas & Propagation*, 12(5), 672–677. <https://doi.org/10.1049/iet-map.2017.0467>
- Kiani, S. H., Alharbi, A. G., Khan, S., Marey, M., Mostafa, H., & Khan, M. A. (2022). Wideband three loop element antenna array for future 5G mmWave devices. *IEEE Access*, 10, 22472–22479. <https://doi.org/10.1109/access.2022.3152769>
- Kildal, P.-S., & Rosengren, K. (2004). Correlation and capacity of MIMO systems and mutual coupling, radiation efficiency, and diversity gain of their antennas: Simulations and measurements in a reverberation chamber. *IEEE Communications Magazine*, 42(12), 104–112. <https://doi.org/10.1109/mcom.2004.1367562>
- Li, Z., Du, Z., Takahashi, M., Saito, K., & Ito, K. (2012). Reducing mutual coupling of MIMO antennas with parasitic elements for mobile terminals. *IEEE Transactions on Antennas and Propagation*, 60(2), 473–481. <https://doi.org/10.1109/tap.2011.2173432>
- Luo, Y., Shen, Y., Cai, X., Qian, F., Xu, S., Cui, H., & Yang, G. (2022). Substrate integrated coaxial line design for mmWave antenna with multilayer configuration. *International Journal of RF and Microwave Computer-Aided Engineering*, 32(5), e23090. <https://doi.org/10.1002/mmce.23090>
- Madni, A., Bilal, R. M. H., & Khan, W. T. (2022). A compact metamaterial-based high-isolation MIMO antenna for 5.8 GHz WLAN applications. In *2022 IEEE international symposium on antennas and propagation and USNC-URSI radio science meeting (AP-S/URSI)*, Denver, CO, USA (pp. 245–246).
- Munir, M. E., Kiani, S. H., Savci, H. S., Marey, M., Khan, J., Mostafa, H., & Parchin, N. O. (2023). A four element mm-wave MIMO antenna system with wide-band and high isolation characteristics for 5G applications. *Micromachines*, 14(4), 776. <https://doi.org/10.3390/mi14040776>
- Pan, Y. M., Qin, X., Sun, Y. X., & Zheng, S. Y. (2019). A simple decoupling method for 5G millimeter-wave MIMO dielectric resonator antennas. *IEEE Transactions on Antennas and Propagation*, 67(4), 2224–2234. <https://doi.org/10.1109/tap.2019.2891456>
- Qasem, N. (2024). Measurement and simulation for improving indoor wireless communication System performance at 2.4 GHz by modifying the environment. *IEEE Access*, 12, 96660–96671. <https://doi.org/10.1109/access.2024.3426490>
- Rafique, U., Khan, S., Ahmed, M. M., Kiani, S. H., Abbas, S. M., Saeed, S. I., et al. (2022). Uni-planar MIMO antenna for sub-6 GHz 5G mobile phone applications. *Applied Sciences*, 12(8), 3746. <https://doi.org/10.3390/app12083746>
- Sehrai, D. A., Abdullah, M., Altaf, A., Kiani, S. H., Muhammad, F., Tufail, M., et al. (2020). A novel high gain wideband MIMO antenna for 5G millimeter wave applications. *Electronics*, 9(6), 1031. <https://doi.org/10.3390/electronics9061031>

- Sharma, A., Rai, J. K., & Katiyar, H. (2023). Design of a high gain MIMO dielectric resonator antenna for 5G mm-wave applications. In *Proceedings of the International Conference on IoT, Communication and Automation Technologies (ICICAT)* (pp. 1–5).
- Shen, X., Liu, Y., Zhao, L., Huang, G. L., Shi, X., & Huang, Q. (2019). A miniaturized microstrip antenna array at 5G millimeter-wave band. *IEEE Antennas and Wireless Propagation Letters*, 18(8), 1671–1675. <https://doi.org/10.1109/lawp.2019.2927460>
- Singh, M., & Parihar, M. S. (2023). Gain improvement of Vivaldi MIMO antenna with pattern diversity using bi-axial anisotropic metasurface for millimeter-wave band application. *IEEE Antennas and Wireless Propagation Letters*, 22(3), 621–625. <https://doi.org/10.1109/lawp.2022.3220710>
- Sokunbi, O., & Attia, H. (2020). Highly reduced mutual coupling between wideband patch antenna array using multiresonance EBG structure and defective ground surface. *Microwave and Optical Technology Letters*, 62(4), 1628–1637. <https://doi.org/10.1002/mop.32193>
- Sokunbi, O., Attia, H., Hamza, A., Shamim, A., Yu, Y., & Kishk, A. A. (2023). New self-isolated wideband MIMO antenna system for 5G mm-wave applications using slot characteristics. *IEEE Open Journal of Antennas and Propagation*, 4, 81–90. <https://doi.org/10.1109/ojap.2023.3234341>
- Sun, Y., Cai, B., Yang, L., Wu, L., Cheng, Y., Luo, H., et al. (2024). High-gain dual-polarization microstrip antenna based on transmission focusing metasurface. *Materials*, 17(15), 3730. <https://doi.org/10.3390/ma17153730>
- Tariq, S., Naqvi, S. I., Hussain, N., & Amin, Y. (2021). A metasurface-based MIMO antenna for 5G millimeter-wave applications. *IEEE Access*, 9, 51805–51817. <https://doi.org/10.1109/access.2021.3069185>
- Tian, H. W., Zhang, X. G., Jiang, W. X., Li, X., Liu, Y. K., Qiu, C., & Cui, T. J. (2021). Programmable controlling of multiple spatial harmonics via a nonlinearly phased grating metasurface. *Advanced Functional Materials*, 32(31), 2203120. <https://doi.org/10.1002/adfm.202203120>
- Yusuf Onay, M., & Dokmetas, B. (2025). 3D Printed microstrip antenna for symbiotic communication: WiFi backscatter and bit rate evaluation for IoT. *Internet of Things*, 32, 101643. <https://doi.org/10.1016/j.iot.2025.101643>
- Zhang, Y., Deng, J. Y., Li, M. J., Sun, D., & Guo, L. X. (2019). A MIMO dielectric resonator antenna with improved isolation for 5G mm-wave applications. *IEEE Antennas and Wireless Propagation Letters*, 18(4), 747–751. <https://doi.org/10.1109/lawp.2019.2901961>